International Journal of Heat and Mass Transfer 270 (2026) 129228

Contents lists available at ScienceDirect

International Journal of Heat and Mass Transfer

journal homepage: www.elsevier.com/locate/hmt

Multi-phase and multi-species decomposition model for hydrogen peroxide in catalytic chambers

Nora M. Riedel [a,*], Christopher Glaser [a], Christian Mundt [b]

[a] Responsive Space Cluster Competence Center, German Aerospace Center (DLR), Eugen-Sänger-Str. 50, Faßberg, D-29328, Germany
[b] Faculty of Aerospace Technology, Institute for Thermodynamics, Universität der Bundeswehr München, Werner-Heißenberg-Weg 39, Neubiberg, D-85577, Germany

ARTICLE INFO

Keywords:
Hydrogen peroxide
Catalytic decomposition
Hybrid rocket engine
Lagrangian approach

ABSTRACT

A mathematical model of the flow through a catalytic chamber to be used in rocket engines is presented. The model is based on a Lagrangian approach and a homogeneous description of the phases. The equation for the decomposition process is expanded to consider the pressure influence on the chemical reaction and the influence of the mass transfer effects (diffusion, adsorption and desorption). For the vaporization and the temperature determination the enthalpy is used. The pressure drop is calculated through a relation between the resistance coefficient and Reynolds number. Polynomial approaches are applied for the thermodynamic and transport properties. The heat transfer between the flow and the chamber wall as well as the flow and the catalytic material is considered. Finally, a comparison between the experimental test data and the simulation results is provided. The steady state values of temperature and pressure match the experimental data. The temperature data are in a range of 8 K, while the pressure data are in the uncertainty of the pressure sensors (±1 bar). The transient behavior of the model shows a good agreement with the experimental data.

1. Introduction

Catalytic chambers are filled with catalytic material. Here the chamber is used to decompose the hydrogen peroxide into oxygen and water vapor. In monopropellant rockets, the catalytic chamber with a nozzle produces the thrust. In hybrid rocket engines, it is positioned in front of the combustion chamber that holds the fuel. Thus the decomposition products are injected directly.

A typical catalytic chamber design is shown in Fig. 1. It consists of two holding plates (gray) between which the catalytic bed with the catalytic material is arranged (light blue circles). Sometimes an injector (yellow) is used to give the exiting flow a specific direction. At the inlet, the hydrogen peroxide is liquid, and at the outlet the hydrogen peroxide is decomposed.

Hydrogen peroxide gains importance for rocket engines because of its environmental friendly properties [1]. It is nontoxic and non-carcinogenic [2,3]. Therefore, the handling of hydrogen peroxide is less complicated, given that some general rules are respected. Besides the environmental friendliness, the high volume specific impulse is another advantage [1]. Due to the high density (1.45 g cm^{-3} [4]) it is possible to use small tanks and overall compact systems. Hydrogen peroxide is not cryogenic, thus it can be stored for many years in a controlled environment (see also [4,5]). Through the reaction heat of the decomposition, the system auto-ignites. In addition, re-ignition of the engine is possible and the system is less complex compared to a system with igniter [2].

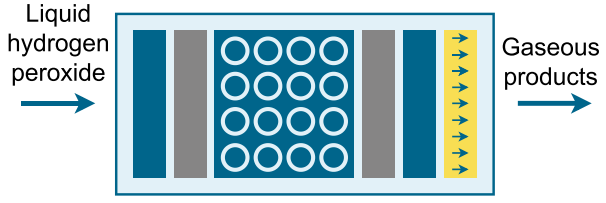

Fig. 1. Schematic design of a generic cylindrical catalytic chamber.

The performance prediction of catalytic chambers under real application conditions is the main goal of the developed tool in this article. With it, the chamber design can be optimized and the development of new configurations is possible.

First, an overview of the state of the art of existing models is given. Then, the methodology is explained. After, the experimental set-up is shortly described. Finally, the model is validated with experimental results and some considerations to the pressure influence are discussed.

* Corresponding author.
E-mail address: nora.riedel@dlr.de (N.M. Riedel).

https://doi.org/10.1016/j.ijheatmasstransfer.2026.129228
Received 7 November 2025; Received in revised form 7 June 2026; Accepted 27 June 2026
Available online 6 July 2026

2. State of the art of decomposition models

Many gaps are still to be closed in modeling of hydrogen peroxide decomposition [6]. A simple homogeneous model was developed by Pasini et al. [7]. This model has a detailed reaction description with adsorption and desorption as well as diffusion limitation. However, the pressure drop calculation deviates from the experimental data [8]. Later the model was extended to include uncertainty [9] and a new pressure drop model [10]. Koopmans et al. [11,12] developed a heterogeneous model with a more detailed pressure drop calculation and a reduced reaction description. Diffusion limitation is not considered in their model. The heat transfer between the catalytic material and the flow is neglected. All models mentioned above assume a steady state of the flow.

Reid et al. [13] developed a transient heterogeneous model. This has a similar detail of the reaction mechanism compared to Refs. [7,11] but without adsorption and desorption. However, it included a new diffusion limitation description. The heterogeneous characteristic of the model refers to the distinction between the solid phase of the catalyst and the flow. The flow itself is modeled homogeneously. It stresses the importance of diffusion limitation although there is no experimental validation of their model yet.

In addition to the detailed simulation models also straight-forward pre-design models exists. One example is the model of Granado et al. [14] which has a 0-dimensional model approach and calculates the exit temperature and a pressure drop. For the mass flow rate a single equation is used.

This article presents an extended version of our own model from [15]. The main modification is the pressure correction of the reaction velocity due to the high catalytic chamber pressures. Moreover, the description of diffusion, adsorption and desorption has been added.

In contrast to the models in the literature, the present model has the capability to simulate the transient behavior. Therefore, it uses the Lagrangian approach for the start up process. Furthermore, it is to the knowledge of the authors the first model which considers the pressure influence on the reaction velocity which allows the experimental validation with data from engines with high mass flow and high chamber pressures. In addition, the model considers the heat exchange between the flow and the catalytic material as well as between the flow and the chamber wall. For the pore diffusion, the impact of bubble evolution for high concentrations is considered for the first time in a decomposition model.

3. Methodology

In the catalytic chamber, the liquid hydrogen peroxide (H_2O_2[1]) is decomposed in gaseous oxygen (O_2) and water vapor (H_2O) [2]

$$2H_2O_2 \rightarrow 2H_2O + O_2 \quad \Delta h_{rkt} = -196.14 \text{ kJ/2mol}. \tag{1}$$

The hydrogen peroxide decomposition is an exothermic process. To reduce the high activation energy a catalyst is used [16]. Therefore, in the present work, an aluminum oxide pallet is considered which is covered with platinum.

The flow in the catalytic chamber is a multi-phase and multi-species flow [17], because the exothermic decomposition process energizes the liquid hydrogen peroxide to gaseous products. Consequently, the vaporization of the liquid needs to be considered. The solid catalyst is treated as steady.

The second aspect – multi-species flow – describes the presence of more than one species [18]. Table 1 summarizes the species and their possible phases.

Several analytical concepts to describe the multi-phase flow exist. The two-fluid approach is the most realistic one. It models the phases separately, for each phase three equations exist: one equation for mass, momentum and energy, respectively. Additionally, there are closing equations called jump-conditions [19]. A less complex approach is the homogeneous model. It is a pseudo-fluid consideration which uses averaged flow parameters [19]. Therefore, the number of equations is reduced to the three conservation equations.

Table 1
Considered phases and species in the catalytic chamber.

Species	Liquid	Gaseous
H_2O_2	x	x
H_2O	x	x
O_2		x

The interfaces between the two phases involve many physical and chemical effects which are often unknown even until today [17]. Therefore, in this article, a homogeneous model with some simplifications (see Section 3.4) is used. The Eqs. (2) to (5) show the general conservation equations for a one-dimensional, homogeneous flow. The first equation is for global mass conservation, the second for the continuity for the species mass, the third for momentum conservation and the fourth for energy conservation [20]:

$$\frac{\partial}{\partial t}\rho_m + \frac{\partial}{\partial x}\rho_m v_m = 0\,, \tag{2}$$

$$\frac{\partial}{\partial t}\alpha\rho_g + \frac{\partial}{\partial x}\alpha\rho_g v_m = \Gamma\,, \tag{3}$$

$$\frac{\partial}{\partial t}\rho_m v_m + \frac{\partial}{\partial x}\rho_m v_m^2 = -\frac{\partial p}{\partial x} + \frac{\partial \tau}{\partial x}\,, \tag{4}$$

$$\frac{\partial}{\partial t}\rho_m h_m + \frac{\partial}{\partial x}\rho_m h_m v_m = -\frac{\partial q}{\partial x}\,. \tag{5}$$

The density is ρ, the velocity v, the phase ratio α and the enthalpy h. Γ is the generated mass due to the decomposition of the hydrogen peroxide. p is the pressure. The heat flux is q and the shear stress tensor is τ. The subscript m is for the averaged value between the liquid and gas flow and g is for the gaseous flow parameter. The reaction enthalpy h_{rkt} is included in Eq. (5). As simplification to the homogeneous model, the momentum Eq. (4) is replaced with an empirical approach (see Section 3.4).

An averaging method is necessary, so that the mean values of the flow can be studied [20]. An often used method is the Eulerian average. There, time and space coordinates are independent [20]. Another approach is the Lagrangian averaging, which is related to the Lagrangian description of mechanics. The time and space coordinates depend on each other [20]. In this article, a Lagrangian averaging is chosen, because the start of the decomposition is of interest. The model to study is shown in Fig. 2. The time t_1 to t_3 show rising time points ($t_1 < t_2 < t_3$). At every time step an additional particle is added to the chamber, calculated and moves one position forward until it exits the chamber at the right side.

In Fig. 3 the detailed calculation algorithm is shown. First, a new gas and fluid particle is added. The particles are initialized with the starting conditions. Then, the decomposition of the particles is calculated. After, the physical state is checked. It is now possible to calculate the temperature of the particles. Thereafter, the pressure drop can be estimated. Consequently, all unknown parameters are computed, so that the thermodynamic and transport properties of the particles, like density and viscosity, can be determined. Finally, the heat transfer calculation is done and the new positions of the particles are computed. The loop is running through every time step. In Sections 3.1 to 3.6 the main calculations are explained in detail.

3.1. Decomposition of hydrogen peroxide

The global differential equation for the decomposition of hydrogen peroxide (Reaction (1)) is shown in Eq. (6) [16]:

$$\frac{d[H_2O_2]}{dt} = -k \cdot [H_2O_2]\,. \tag{6}$$

[1] See Nomenclature at end of paper.

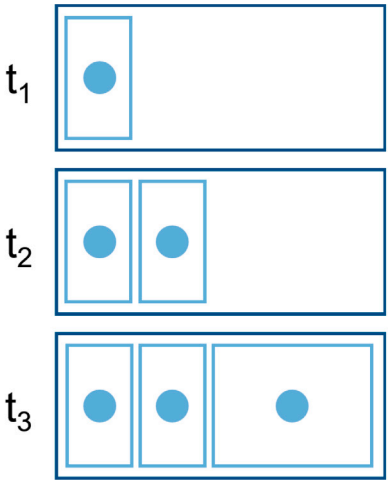

Fig. 2. Lagrangian flow model.

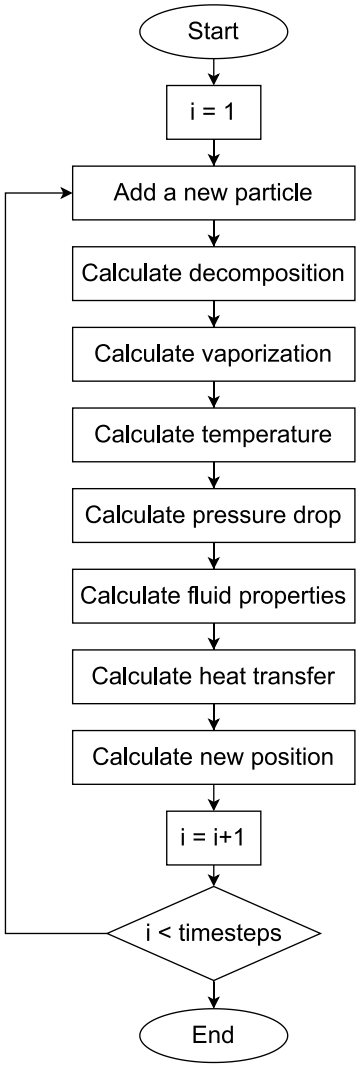

Fig. 3. Algorithm.

$[H_2O_2]$ is the molar concentration of the hydrogen peroxide. k is the reaction velocity, which has a temperature dependency, described by the Arrhenius equation [16]:

$$k = A \cdot e^{\frac{-E_a}{RT}} . \tag{7}$$

In Eq. (7), the symbol A is the pre-exponential factor, E_a the activation energy, R the universal gas constant and T denotes the temperature. Additionally to the temperature influence on the reaction velocity k (see Eq. (7)), the following impacts are considered in this article and explained below: pressure, condition of the catalytic material, external diffusion, internal diffusion, adsorption and desorption process.

The reaction velocity of palladium catalysts has both a pressure and a temperature dependency [21]. According to the principle of Le Chatelier [16], the reaction velocity in Reaction (1) reduces at higher pressures. Chemically, the relation of Planck and van Laar (Eq. (8)) describes the pressure (p) influence on the chemical equilibrium constant (K) [22]. $\Delta V°$ is the reaction volume and can be calculated for an ideal gas mixture with Eq. (9) [22]. It depends on the stoichiometric coefficients ν_r of the reaction:

$$\left(\frac{\partial \ln K}{\partial p}\right) = -\frac{\Delta V°}{RT} , \tag{8}$$

$$\Delta V° = \frac{RT}{p} \sum_r \nu_r . \tag{9}$$

Eqs. (8) and (9) applied on Reaction (1) results in Eq. (10). Now, the chemical equilibrium constant (K) at different pressures can be calculated. From the chemical equilibrium constant at pressure K_2 a proportional correction of the reaction velocity k is made:

$$\ln K_2 = -\frac{p_2 - p_1}{2p_2} + \ln K_1 . \tag{10}$$

The influence of the pressure on the simulation results can be seen in Section 5.1.

The reaction velocity k is an experimental measured value. It depends on temperature, the catalytic material quantity and the catalytic material preparation. A common evaluation criterion for the catalytic material preparation is the BET (Brunauer, Emmett and Teller [23]) area. The three aspects (temperature, catalytic material quantity and preparation) are considered through a correction factor [24].

For the mass transfer, a boundary layer is formed on the outer surface of the catalytic material [6]. The transport through this boundary layer is called external diffusion. After this, the pore diffusion in the pores of the catalytic material takes place. Then, the hydrogen peroxide has to be adsorbed from the active area of the catalytic material. Now, the chemical decomposition takes place (Reaction (1)). After, the reaction products run through the process backwards: desorption, pore diffusion and external diffusion. The whole process is shown in Fig. 4.

The external diffusion coefficient η_{ex} for high hydrogen peroxide concentrations can be assumed equal to one [25]. The pore diffusion coefficient η_{pore} can be calculated based on two methods. The Thiele module [26] is used for small hydrogen peroxide concentrations. For high hydrogen peroxide concentrations an approach from Ref. [25] is used which considers the bubble evolution. The Thiele module (ϕ) for spherical particles can be calculated with [26]:

$$\phi = \frac{1}{3} r_{\text{cat}} \sqrt{k / D_{\text{eff}}} , \tag{11}$$

$$D_{\text{eff}} = \frac{\varepsilon}{\tau^2} D . \tag{12}$$

r_{cat} is the radius of the catalyst particles, D the diffusion coefficient and τ the tortuosity of the material. The pore efficiency is then [26]:

$$\eta_{\text{pore},T} = \frac{\tanh \phi}{\phi} . \tag{13}$$

The calculation of the pore diffusion coefficient ($\eta_{\text{pore},B}$) from Ref. [25] is based on the assumption that the rate of reaction in a pore is equal to the rate of diffusion out of the pore. For the calculation, the mean pore diameter of the catalyst has to be determined in the laboratory with

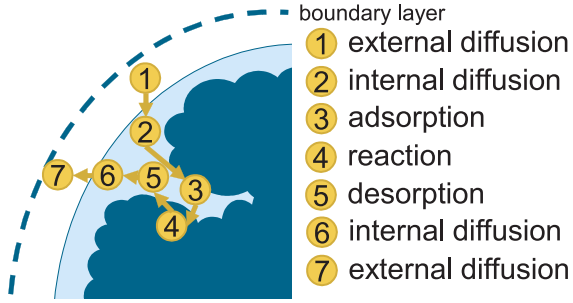

Fig. 4. Mass transfer process of the heterogeneous catalyst reaction based on [6].

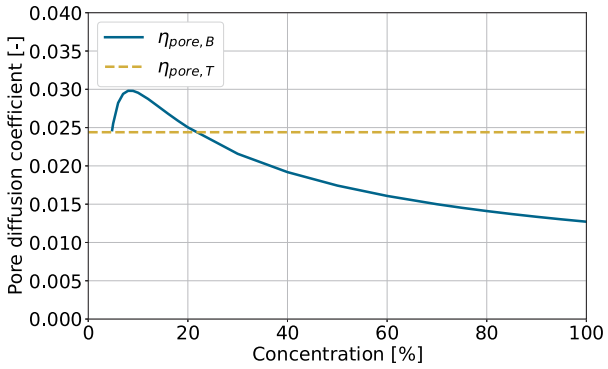

Fig. 5. Pore diffusion coefficient of Thiele and Bubble over the concentration of hydrogen peroxide.

Table 2
Efficiency coefficient on the reaction velocity due to mass transfer.

Mass transfer	Coefficient	Value
External diffusion	η_{ext}	constant
Pore diffusion (low concentrations)	$\eta_{pore,T}$	calculated
Pore diffusion (high concentrations)	$\eta_{pore,B}$	calculated
Adsorption/desorption	n_u	calculated

a gas adsorption and a subsequent BJH (Barrett, Joyner and Halenda) method [27]. Both pore diffusion coefficients are shown in Fig. 5. It is noticeable that the Thiele coefficient ($\eta_{pore,T}$) is not concentration dependent while the Bubble coefficient ($\eta_{pore,B}$) depends on it.

A standardization is used for η_{pore} to adapt the literature values of k to the one used in this article.

For the inclusion of the adsorption and desorption the Langmuir equation [16] is used:

$$\Theta = \frac{K \cdot C}{1 + K \cdot C} = \frac{n_u}{n_a} . \tag{14}$$

C is the weight percent concentration of hydrogen peroxide. Θ is a value for the ratio of the number of used adsorption places n_u to the number of available adsorption places n_a. Converted to n_u, the adsorption efficiency coefficient depends on:

$$n_u = n_a \Theta . \tag{15}$$

The value n_a is integrated in the pre-exponential factor A [12]. The value Θ can be calculated with the known values, K and C. A summary of the efficiency coefficients due to the mass transfer is shown in Table 2.

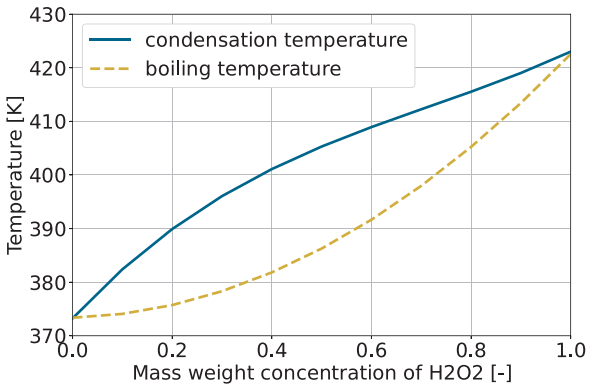

Fig. 6. Phase diagram of hydrogen peroxide for a pressure of 1 bar [15].

In the reaction model, only the catalytic decomposition is considered. The thermal decomposition of hydrogen peroxide is neglected and can be considered with a second reaction velocity for the thermal decomposition process.

Additional to the change of mole fraction of the hydrogen peroxide, the reaction enthalpy:

$$h_{rkt} = 28.83 \text{ kJ/kg C} , \tag{16}$$

is added to the actual enthalpy of the particle. It depends on the weight percent concentration (C) of the hydrogen peroxide and is important for the temperature calculation later (Section 3.3). The Eq. (16) assumes for the complete decomposition of 100% hydrogen peroxide a reaction enthalpy of 689 cal/g [2]. This corresponds to an enthalpy of 2882.8 kJ/kg. For a concentration of 0% a reaction enthalpy of 0 kJ/kg is assumed. A linear interpolation for the other concentrations is considered.

3.2. Vaporization

For the vaporization process a categorization of the particles is carried out. The enthalpy of each particle is categorized in the pressure corrected phase diagram of hydrogen peroxide (see Ref. [15]). The phase diagram for a pressure of 1 bar is shown in Fig. 6 [28]. If the enthalpy is below the boiling enthalpy the particle is still liquid ($\alpha = 0$). If the enthalpy is higher than the condensation enthalpy the particle is fully gaseous ($\alpha = 1$). If the enthalpy is between the boiling and the condensation enthalpy, the particle has two phases and the phase ratio α is between 0 and 1. Depending on the categorization, a different temperature calculation procedure is selected. It should be mentioned that the oxygen is always gaseous independent from α.

3.3. Temperature

The temperature calculation is based on the enthalpy. For the fully liquid particle ($\alpha = 0$) the enthalpy is composed of the enthalpy of formation h_0 and the enthalpy of the mass fraction at the current temperature calculated with the specific heat capacity (see Eq. (17)) [16]:

$$h_I = h_0 + mf_{H_2O_2} \cdot \int_{T_0}^{T_I} c_{p,H_2O_2,l} \mathrm{dT} + mf_{H_2O} \cdot \int_{T_0}^{T_I} c_{p,H_2O,l} \mathrm{dT} + mf_{O_2} \cdot \int_{T_0}^{T_I} c_{p,O_2} \mathrm{dT} . \tag{17}$$

For $\alpha = 1$ (fully gaseous) the enthalpy is dependent on the enthalpy of condensation h_{cond} and the enthalpy of the mass fraction at the

current temperature calculated with the specific heat capacity (see Eq. (18)) [16]:

$$h_{III} = h_{\text{cond}} + mf_{H_2O_2} \cdot \int_{T_{\text{cond}}}^{T_{III}} c_{p,H_2O_2,g}\mathrm{dT} + mf_{H_2O} \cdot \int_{T_{\text{cond}}}^{T_{III}} c_{p,H_2O,g}\mathrm{dT} + mf_{O_2} \cdot \int_{T_{\text{cond}}}^{T_{III}} c_{p,O_2}\mathrm{dT} \,. \tag{18}$$

For the two-phase particle (Eq. (19)), the enthalpy additional depends on the phase ratio and enthalpy of vaporization H_V. The starting point is the enthalpy of the temperature T_{boil}, where the vaporization of the liquid starts (h_{boil}). For the solution of the equation a zero-point method is used. Therefore, the enthalpy of the particle is subtracted from Eqs. (17) and (18). Then, the new equation can be solved for $\alpha = 0$ (fully liquid) and $\alpha = 1$ (fully gaseous) with a Newton's method [29]. For the two-phase particle a bisection method [29] is used to find the new temperature iteratively (see also Ref. [15]):

$$\begin{aligned} h_{II} = {} & h_{\text{boil}} + mf_{H_2O_2} \cdot (1-\alpha) \cdot \int_{T_{\text{boil}}}^{T_{II}} c_{p,H_2O_2,l}\mathrm{dT} \\ & + mf_{H_2O_2} \cdot \alpha \cdot \left[H_{V,H_2O_2} + \int_{T_{\text{boil}}}^{T_{II}} c_{p,H_2O_2,g}\mathrm{dT}\right] \\ & + mf_{H_2O} \cdot (1-\alpha) \cdot \int_{T_{\text{boil}}}^{T_{II}} c_{p,H_2O,l}\mathrm{dT} \\ & + mf_{H_2O} \cdot \alpha \cdot \left[H_{V,H_2O} + \int_{T_{\text{boil}}}^{T_{II}} c_{p,H_2O,g}\mathrm{dT}\right] \\ & + mf_{O_2} \cdot \int_{T_{\text{boil}}}^{T_{II}} c_{p,O_2}\mathrm{dT} \,. \end{aligned} \tag{19}$$

The enthalpy h_{boil} and h_{cond} describe the two-phase area according to Fig. 6.

3.4. Pressure

The law of resistance is the relation between the resistance coefficient Ψ and the Reynolds number Re [30]. For packed catalyst beds, the resistance coefficient is defined as shown in Eq. (20). The Reynolds number for particles is defined in Eq. (21):

$$\Psi \equiv \frac{\varepsilon^3}{1-\varepsilon} \frac{\Delta p}{\rho v^2} \frac{d_{\text{cat}}}{l} \,, \tag{20}$$

$$Re \equiv \frac{v\, d_{\text{cat}}}{\nu} \cdot \frac{1}{1-\varepsilon} \,. \tag{21}$$

ε is the void fraction, ρ the density, d_{cat} the catalytic particle diameter, v the velocity, ν the kinematic viscosity and Δp the pressure drop. The laws of resistance are empirical estimations [30]. Ergun [31] established a relation between the two numbers for granule layers:

$$\Psi = \frac{150}{Re} + 1.75 \,. \tag{22}$$

Tallmadge [32] modified the empirical constants 150 and 1.75 of Eq. (22) for high Reynolds numbers, the approach was often discussed in the past (see Ref. [33]):

$$\Psi = \frac{150}{Re} + \frac{4.2}{Re^{1/6}} \,. \tag{23}$$

Wu et al. [33] developed a model, which replaces the empirical constants by two expressions with a clear physical meaning. These expressions are based on the average hydraulic radius model and the contracting-expanding channel model [33]. The relation is shown in Eqs. (24)–(27):

$$\Psi = \frac{71\tau}{Re} + \frac{3\tau\left[(3/2) + (1/\beta^4) - (5/2\beta^2)\right]}{4} \,, \tag{24}$$

$$\tau = \frac{1}{2}\left[1 + \frac{1}{2}b + b\frac{\sqrt{(1/b-1)^2 + (1/4)}}{1-b}\right] \,, \tag{25}$$

$$b = \sqrt{1-\varepsilon} \,, \tag{26}$$

$$\beta = 1/(1-b) \,. \tag{27}$$

The tortuosity (τ) can be computed with Eq. (25). The shape parameter (β) is calculated with Eq. (27). With some mathematical modifications of Eq. (20) and (24) the pressure drop (Δp) can be calculated.

3.5. Thermodynamic and transport properties

For the different flow parameters, like density, thermal conductivity, viscosity and heat capacity, standard equations are used A. First, the parameter for each species in each phase is calculated. Then, averaged parameter values are computed with the mass fractions of the species for the two phases.

3.6. Heat transfer

According to the first law of thermodynamics, heat is the energy which is carried over the system border due to temperature difference [34]. In general, there are three kinds of heat transfer: heat conduction, heat convection and heat radiation. The heat conduction is a diffuses energy transfer between two particles [34]. In the model heat conduction is only considered in the wall (see Section 3.6.1). The convective heat transfer requires the movement of a medium [34]. This heat transfer is considered between the flow and the wall (see Section 3.6.1) as well as the flow and the catalytic material (see Section 3.6.2). Heat of radiation is caused by electromagnetic waves [34]. This heat transfer mechanism is not considered in the model, because of relatively low temperatures.

After the rates of heat are computed, the new enthalpy of the particle can be calculated. This is shown in Eq. (28):

$$h_{\text{new}} = h - \frac{\dot{Q}_{\text{conv,wall}} + \dot{Q}_{\text{conv,cat}}}{\dot{m}} \,. \tag{28}$$

3.6.1. Wall heat transfer

The wall of the catalytic chamber has a convective heat transfer with the flow:

$$\dot{Q}_{\text{conv, wall}} = d_i \cdot \pi \cdot \Delta pp \cdot \alpha \cdot (T - T_{\text{wall}}) \,. \tag{29}$$

Hereby d_i is the inner wall diameter and Δpp the position of the particle alongside the wall. The heat transfer coefficient α depends not only on the material but also on the flow condition. It is computed with Eq. (30) [34]. Nu is the dimensionless Nusselt number which is calculated for the flow in packed catalyst beds (see also [34]). The thermal conductivity λ_{tot} is known from Section 3.5 and d_{cat} is the diameter of the catalyst particle. The temperature difference in Eq. (29) is between the flow temperature T and the wall temperature T_{wall}:

$$\alpha = \frac{Nu \cdot \lambda_{\text{tot}}}{d_{\text{cat}}} \,. \tag{30}$$

At the beginning, the wall temperature is at ambient temperature. Through conduction the temperature changes. Therefore, the averaged particle temperature from the particle based coordinate system is transformed to the wall cylindrical coordinate system. The different coordinate systems are shown in Fig. 7. Then, the heat conduction equation (Eq. (31)) [34] is computed with the Crank–Nicolson method and the Thomas algorithm [35]. Afterwards the coordinate transformation is reversely calculated and T_{wall} is known:

$$\frac{\partial T}{\partial t} = q \cdot \left(\frac{\partial^2 T}{\partial x^2} + \left(\frac{r_{i+1}}{r_i}\right)^2 \cdot \frac{\partial^2 T}{\partial r^2}\right) \,, \tag{31}$$

$$q = \frac{\lambda}{\rho\, c_p} \,. \tag{32}$$

As the catalytic chamber wall is a cylindrical component the equation has a correction factor in r-direction. An example segmentation of the wall is shown in Fig. 7.

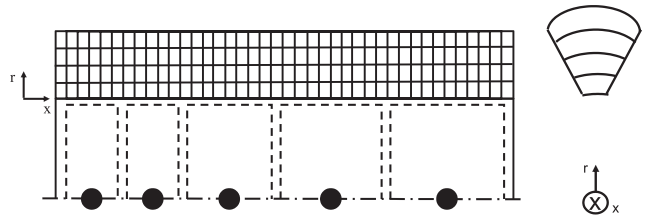

Fig. 7. Wall grid vs. particle system.

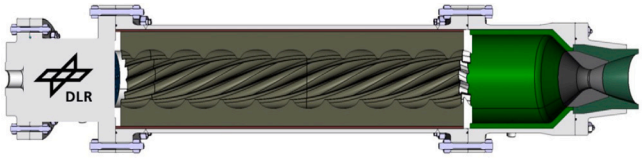

Fig. 8. CAD model of the VISERION engine [38].

Table 3
Input values from the test data.

Parameter	Engine test	Catalytic chamber test
Mass flow rate	5 kg/s	4.8 kg/s
HTP concentration	88.2%	87.9%
Calculated inlet pressure	58 bar	67 bar
Environment temperature	21.6 °C	18.7 °C

3.6.2. Convective heat transfer with the catalyst material

The convective heat transfer between the catalyst material and the flow can be computed with Eq. (33). The contact area between the catalyst particles and the flow is given through the ratio between the surface and the volume of the particles ($6 \cdot m_{cat}/d_p \cdot \rho_p$). m_{cat} is the mass of catalyst and ρ_{cat} is the catalyst density:

$$\dot{Q}_{conv,\ cat} = \frac{6 \cdot m_{cat}}{d_{cat} \cdot \rho_{cat}} \cdot \alpha \cdot (T - T_{cat}) \,. \tag{33}$$

At the beginning, the catalyst material is at ambient temperature. With initial condition, the one-dimensional heat equation (compare Eq. (31)) is used to calculate the heating.

4. Experimental set-up

The experimental validation is carried out on the VISERION engine [36]. It is a hybrid rocket engine with a propellant combination of 87.5 wt.% High-Test Peroxide (HTP) and Hydroxyl-Terminated Polybutadiene (HTPB). It has an average thrust of 11.5 kN over 27 s [37]. The engine is shown in Fig. 8 [38]. It consists of the catalytic chamber, the combustion chamber with the fuel, the swirl plate (white), the post-combustion chamber (green) and the nozzle throat (gray). The test data from two test campaigns are used in this article. First, a catalytic chamber test is shown in Fig. 9. This was a catalytic chamber test without the HTPB block to validate the performance of the catalytic chamber. Additionally, the data of one full engine test (see Fig. 10) are used. From this test, the thrust, mass flow, combustion chamber pressure and catalytic chamber exit temperature over time are shown in Fig. 11. Characteristic values of both tests are presented in Table 3. These are used as input for the tool.

The outer hull of the catalytic chamber for the chamber test and the engine test is different. In the engine test the hull is more heavy, because it is the test bench configuration. The hull of the catalytic chamber test is lighter due to the planned use in a flight engine. The

Fig. 9. Catalytic chamber test of the VISERION engine.

Fig. 10. Full engine test of the VISERION engine [36].

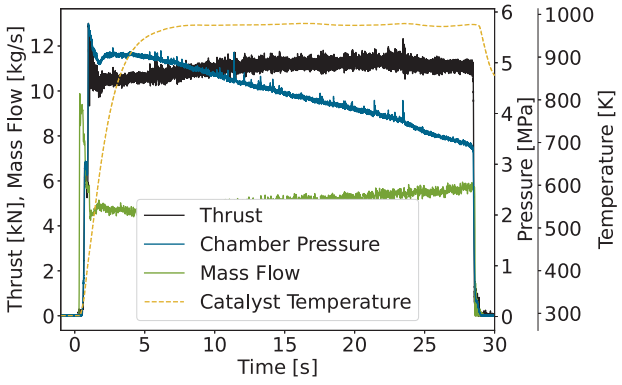

Fig. 11. Measured data during the VISERION engine test [36].

inner catalytic chamber design is equal for both tests and corresponds to the schematic design of Fig. 1. The catalyst bed is filled with commercial granules of aluminium oxide pellets which are coated with platinum resulting in a 5 weight percent platinum content. The average particle diameter is 1.7 mm. The catalyst bed loading (CBL) is defined in Ref. [39]:

$$CBL = \frac{\dot{m}}{A} \,. \tag{34}$$

For both tests, the CBL is approximately 277 kg/s m^2 which is a relative high value compared to other literature values (for example in Ref. [39]). This is due to the application of the catalytic chamber in a

Table 4
Input values from the catalyst.

Parameter	Value
Support material	aluminium oxide
Catalyst material	5% platinum
Shape	granules
Averaged diameter	1.7 mm
Reaction velocity	0.0015 $m^3/s\,kg$
Activation energy	49 kJ/mol

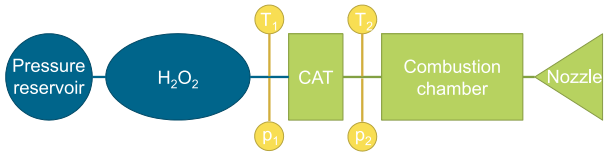

Fig. 12. Overview of the experimental set-up.

hybrid rocket engine instead of a monopropellant thruster. The input parameters for the simulation are shown in Table 4. The value for the reaction velocity and the activation energy is taken from Ref. [24].

The fluid system (blue) and the VISERION engine (green) is schematically shown in Fig. 12. The hydrogen peroxide inside of the vessel is pressurized and transported into the engine. The VISERION engine consists of the catalytic chamber (CAT), the combustion chamber (including the fuel, swirl plate and post-combustion chamber) and the nozzle. The sensor data before and after the catalytic chamber are recorded. The temperature upstream the catalytic chamber (T_1) corresponds to the environment temperature of the hydrogen peroxide. The temperature downstream the catalytic chamber (T_2) is used for the validation of the simulation. The pressure drop can be calculated with the input pressure (p_1) and the exit pressure (p_2).

5. Results and discussion

In this section, the results are presented and discussed. First, the influence of the pressure on the chemical reaction and the impact on the model is presented. Then, the numerical results are compared to theoretical and experimental results for validation of the accuracy of the model.

5.1. Pressure influence

The influence of the chamber pressure on the reaction velocity k is made with a proportional factor from Eq. (10). The proportional factor for the hydrogen peroxide decomposition is shown in Fig. 13. The influence on the reaction velocity decreases from a factor of 1 at 1 bar to an asymptotic value of 0.6. To evaluate the influence on the model, the difference in exit temperature from a simulation with and without corrected reaction velocity is illustrated in Fig. 14. The final temperature of an adiabatic simulation without pressure correction is 980 K whereby the final temperature of an adiabatic simulation with pressure correction is 986 K. With the pressure correction, the final temperature is increased by 6 K. Secondly, the pressure correction delays the temperature increase by 5 ms. Due to the difference in the final temperature, the pressure correction is considered for the validation cases in this article.

5.2. Validation with experimental data from the VISERION engine

For the validation of the simulation results, temperature and pressure data of the VISERION engine are used. In Fig. 15 a comparison of the simulation (with and without heat transfer) and test data from the VISERION catalytic chamber test for the temperature is shown. The simulation data are shifted along the x-axis by 0.36 s to account

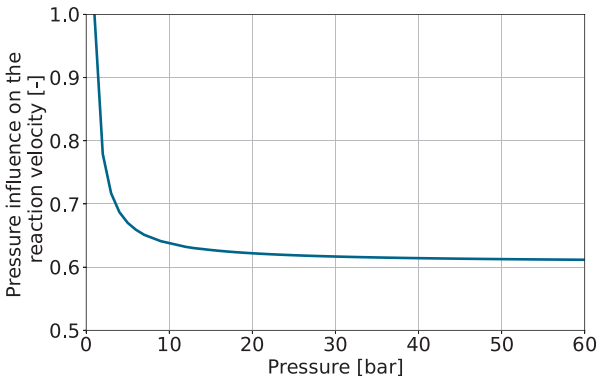

Fig. 13. Pressure influence on the reaction velocity.

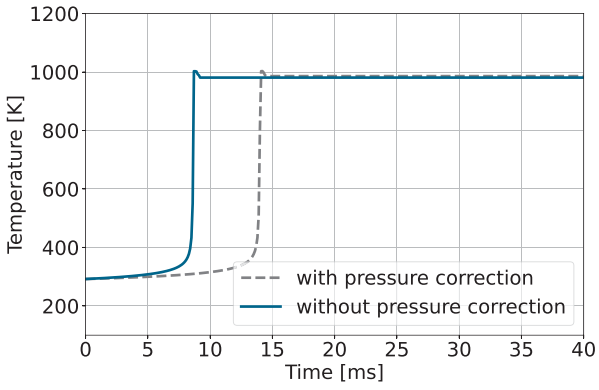

Fig. 14. Pressure influence on the reaction velocity for the adiabatic simulations.

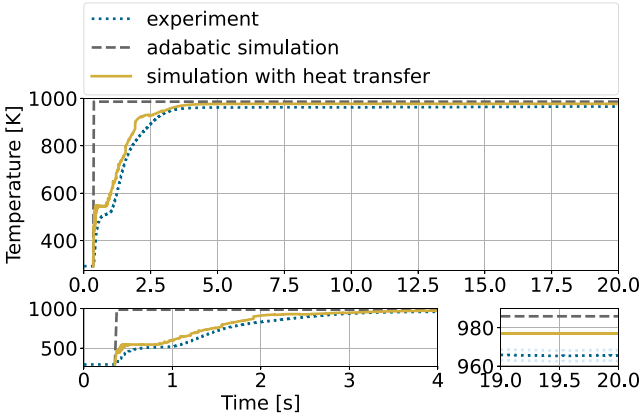

Fig. 15. Temperature (T_2) over time for the experimental and simulation data from the VISERION catalytic chamber test (upper image: full test time, lower images zoomed in sections).

for the main valve actuation time. The blue dotted line represents the experimental data. The adiabatic simulation data are indicated as gray dot-dashed line and the simulation with heat transfer is illustrated as yellow continuous line.

The data of the adiabatic simulation reaches the steady state temperature almost immediately and have no plateau in the beginning (at 1 s), while the data of the simulation with heat transfer shows the plateau. The plateau of the experimental data is suspected to be induced by a ramp up phase at the start of the catalytic decomposition process. In the corresponding time of the test videos (screenshots shown in Fig. 16), a white spray exiting the nozzle is visible. After one second the spray

(a) Shortly after opening of the main valve

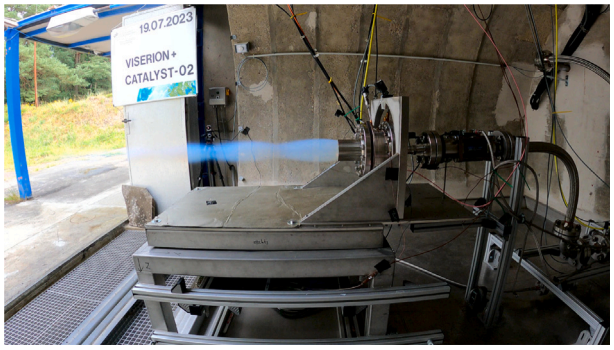

(b) After approximately 1 s

Fig. 16. Screenshot from the test video of the VISERION catalytic chamber test at different times.

Table 5
Catalytic chamber exit temperature.

Scientific method	Catalytic chamber test [K]	Engine test [K]
Experiment	966.0 ± 2.8	975.6 ± 2.8
Adiabatic simulation	985.9	982.8
Simulation with heat transfer	977.0	979.4

becomes less visible and then at 2.5 s it is fully transparent. Thus, the heat exchange model can map the transient behavior.

At the end of the experiment, different exit temperatures (T_2) are reached. These are shown in the center column of Table 5.

The adiabatic simulation exit temperature (T_2) from the catalytic chamber test (Fig. 15) is slightly higher than the theoretical adiabatic decomposition temperatures calculated with the chemical equilibrium with applications code (CEA) [40]. For the catalytic chamber test the theoretical adiabatic temperature is 976.3 K. The difference could be introduced due to the fact that the CEA code has no variation in start enthalpy of hydrogen peroxide for different start temperatures. The final temperature from the catalytic chamber test (Fig. 15) with heat transfer is 20 K lower than the adiabatic simulation. Furthermore, the simulation with heat transfer reaches the final temperature approximately 4 s later compared to the adiabatic one. The difference between the simulation with heat transfer and the experimental results for the catalytic chamber test in the final state is 11 K. It is to be considered that the experimental temperature value is subject to an uncertainty. For a thermocouple element type N [41] the uncertainty over 650 K is calculated with:

$$\pm 0.004 \cdot |T - 273.15\,\mathrm{K}| \,. \tag{35}$$

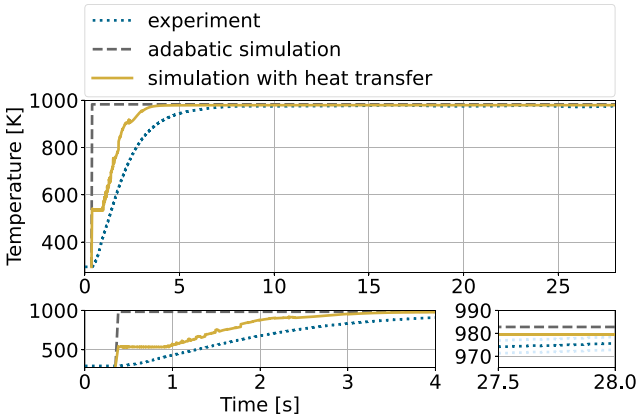

Fig. 17. Temperature (T_2) over time for the experimental and simulation data from the VISERION engine test (upper image: full test time, lower images zoomed in sections).

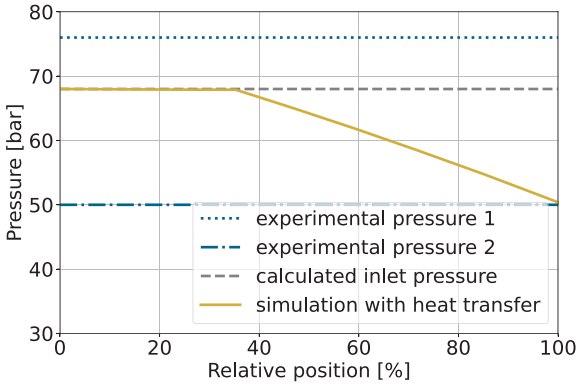

Fig. 18. Pressure vs. position in the chamber from the VISERION catalytic chamber test at 20 s.

Following the uncertainty for the catalytic chamber test can be calculated to ±2.8 K. Considering the uncertainty the experimental temperature and the simulation results have a difference of 8 K.

Generally the behavior of the validation case with the engine test (Fig. 17) is similar to the catalytic chamber test. The experimental data of the VISERION catalytic chamber test (Fig. 15) and engine test (Fig. 17) differs in the temperature rise in the beginning because of two reasons. First, the engine test is done with a catalytic chamber which has a thicker wall, therefore the increase of the temperature is slower in comparison to the catalytic chamber test. Second, the VISERION engine test has no plateau in the temperature increase due to a thicker thermocouple diameter and a related slower reaction time of the thermocouple.

The adiabatic simulation exit temperature (T_2) from the engine test (Fig. 17) is coherent to the theoretical adiabatic decomposition temperatures calculated with the chemical equilibrium with applications code (CEA) [40]. For the engine test the theoretical adiabatic temperature is 984.5 K. The final numerical values are compared to the experimental values in Table 5 in the right column. Considering the uncertainty the experimental temperature and the simulation results with heat transfer concur for the engine test (1 K difference).

Next, the pressure data are investigated. In Fig. 18, the pressure drop vs. the catalytic bed length for the catalytic chamber test is shown. In Table 6 the pressure drop of the simulation and the pressure drop of the experiment are listed in absolute values in the center column. The

Table 6
Pressure drop of the catalytic bed.

Scientific method	Catalytic chamber test [bar]	Engine test [bar]
Experiment	18.5 ± 1.0	15.3 ± 1.0
Simulation	17.6	14.7

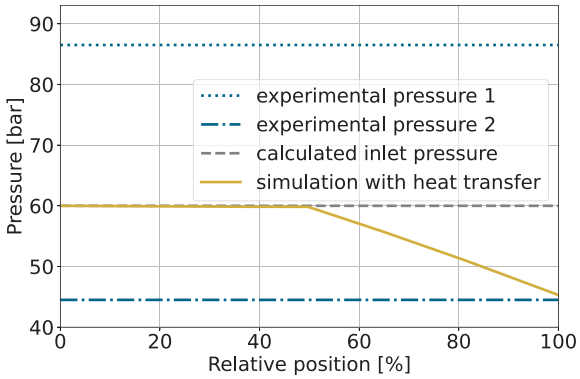

Fig. 19. Pressure vs. position in the chamber from the VISERION engine test at 28 s.

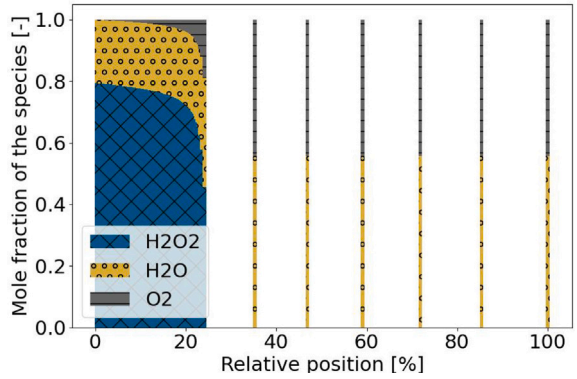

Fig. 20. Mole fraction of the species at different positions in the chamber from the VISERION catalytic chamber test.

experimental pressure drop is calculated with the pressure difference between two pressure sensors (p_1 and p_2 represented by the blue lines in Fig. 18) considering the calculated pressure drop of the inlet plate. The resulting catalytic bed inlet pressure is indicated as gray dashed line. The pressure sensors have an uncertainty of 0.5% of the full scale value therefore the pressure drop value is ±1.0 bar for both tests. Comparing the experimental and the numerical data, the inlet and the outlet pressure values are in good agreement.

The behavior of the pressure for the engine test (Fig. 19) is similar to the catalytic chamber test and maps also the experimental pressure drop (see Table 6).

Since there are no experimental values inside the catalytic bed, they cannot be compared. Thus, the mole fraction of the different species are shown in the bar chart in Fig. 20 to show coherence.

The blue bars represent the hydrogen peroxide mole fractions, the yellow bars the water mole fractions and the gray bars the oxygen mole fractions. All species from Table 1 are taken into account, whereby their state of aggregation is not shown in the diagram. The sum of all mole fraction needs to be one. It should be noted that the distance between the bars is representative for the distance between the calculation points in the chamber. At the entrance of the chamber, a mixture of hydrogen peroxide and water is present. At the exit, the hydrogen peroxide is fully decomposed in water vapor and oxygen. The mole fraction of the VISERION engine test shows a similar behavior. For a more detailed comparison between the experimental and simulation data, a catalytic chamber with sensors in the catalyst bed is planned [42]. In the future, the temperature and pressure values over the chamber length can be compared as well.

6. Conclusion

In this article, the preliminary results from an improved transient decomposition model for hydrogen peroxide is presented. It takes into account multi-species and multi-phase decomposition. The model is suited for high pressure and high mass flow application. It is a homogeneous model and is based on a Lagrangian approach. The mathematical equations used for the calculation of the decomposition, vaporization, temperature, pressure drop, thermodynamic and transport properties and the heat transfer are presented. Some unique features in the simulation are the influence of pressure on the chemical reaction and the detailed heat transfer between the flow and the catalytic material as well as the flow and the wall. Furthermore, the influence of mass transfer on the reaction velocity is considered.

The analysis of the pressure influence on the reaction velocity has revealed that the pressure influence should be taken into account for hydrogen peroxide decomposition models.

The presented model matches steady state experimental data from the hybrid rocket engine VISERION well, both for cases with and without combustion chamber. The transient behavior of the model shows a good agreement with the experimental data, because of the detailed modeling of the heat transfer.

Summarizing, the presented model can be a promising evolution of the decomposition modeling that also considers transient behavior. Its validity has been preliminary proven, but needs to be further evaluated on broader experimental data from inside of the catalytic chamber.

CRediT authorship contribution statement

Nora M. Riedel: Writing – review & editing, Writing – original draft, Visualization, Validation, Software, Resources, Methodology, Investigation, Formal analysis, Data curation, Conceptualization. **Christopher Glaser:** Writing – review & editing, Visualization, Supervision. **Christian Mundt:** Writing – review & editing, Supervision, Methodology.

Declaration of competing interest

The authors declare that they have no known competing financial interests or personal relationships that could have appeared to influence the work reported in this paper.

Acknowledgments

The experimental data of the VISERION engine were generated in co-operation with the department Spacecraft of the DLR Institute of Aerodynamics and Flow Technology, with whom the authors work closely on the research topic of hybrid rocket engines.

Appendix A. Thermodynamic and transport properties calculation

A.1. Density

The density ρ is calculated with the ideal gas Eq. (A.1) [43]:

$$\rho = \frac{p}{T \cdot R_s} \,. \tag{A.1}$$

Hereby, p is the pressure, T the temperature and R_s the specific gas constant.

A.2. Thermal conductivity

The thermal conductivity λ is calculated for each species separately. For water and oxygen, a polynomial approach is used (Eqs. (A.2)) [44]. The coefficients a_1 to a_4 [24] are determined with experimental data from Ref. [45]:

$$\ln(\lambda) = a_1 \cdot \ln(T) + a_2 \cdot T^{-1} + a_3 \cdot T^{-2} + a_4 \,. \tag{A.2}$$

For hydrogen peroxide, an approach and experimental data from Ref. [46] are used. This approach is shown in Eqs. (A.3) and (A.4):

$$\log(\lambda_l) = a_1 + a_2 \cdot \left(1 - \frac{T}{a_3}\right)^{27} , \tag{A.3}$$

$$\lambda_g = a_1 + a_2 \cdot T^{-1} + a_3 \cdot T + a_4 \cdot T^2 \,. \tag{A.4}$$

A.3. Viscosity

The viscosity η is approximated equivalent to the thermal conductivity. The mathematical approach for water and oxygen is shown in Eq. (A.5) [44]. The viscosity of hydrogen peroxide is computed with Eq. (A.6) and (A.7) [46]:

$$\ln(\eta) = b_1 \cdot \ln(T) + b_2 \cdot T^{-1} + b_3 \cdot T^{-2} + b_4 \,, \tag{A.5}$$

$$\log(\eta_l) = b_1 + b_2 \cdot T^{-1} + b_3 \cdot T + b_4 \cdot T^2 \,, \tag{A.6}$$

$$\eta_g = b_1 + b_2 \cdot T^{-1} + b_3 \cdot T + b_4 \cdot T^2 \,. \tag{A.7}$$

A.4. Heat capacity

The heat capacity c_p is represented by a polynomial approach equivalent to the thermal conductivity. The approach is shown in Eq. (A.8) to (A.10) [44,46]. For the calculation of the heat capacity of water and oxygen, pressure depended data from Ref. [45] are used. For the heat capacity of hydrogen peroxide, data at 1 bar are used:

$$c_p = c_1 \cdot T^{-2} + c_2 \cdot T^{-1} + \cdots + c_7 \cdot T^4 \,, \tag{A.8}$$

$$c_{p,l} = c_3 + c_4 \cdot T + c_5 \cdot T^2 + c_6 \cdot T^3 \,, \tag{A.9}$$

$$c_{p,g} = c_3 + c_4 \cdot T + c_5 \cdot T^2 + c_6 \cdot T^3 + c_7 \cdot T^4 \,. \tag{A.10}$$

Appendix B. Nomenclature

Greek symbols

α	Heat transfer coefficient [W/m^{2}K]
α	Phase ratio [–]
β	Shape parameter [–]
ε	Void fraction [–]
η	Efficiency coefficient [–]
η	Viscosity [Pas]
Θ	Occupacy [–]
Γ	Generated specific mass [kg/m^{3}s]
λ	Thermal conductivity [W/mK]
ν	Kinematic viscosity [m^2/s]
ν	Stoichiometric coefficient [–]
ρ	Density [kg/m^3]
τ	Shear stress tensor [N/m^2]
τ	Tortuosity [–]
Φ	Thiele module [1/m]
Ψ	Resistance coefficient [–]

Latin symbols

A	Pre-exponential factor [1/s]
$a_1 - a_4$	Factor [diverse]
$b_1 - b_4$	Factor [diverse]
C	Weight percent concentration [–]
$c_1 - c_7$	Factor [diverse]
c_p	Heat capacity [J/K]
CBL	Catalyst bed load [kg/sm^2]
D	Diffusion coefficient [1/m]
d	Diameter [m]
E_a	Activation energy [J/mol]
h	Specific enthalpy [J/kg]
H_V	Vaporization enthalpy [mol/J]
$[H_2O_2]$	Molar concentration of hydrogen peroxide [mol/m^3]
K	Chemical equilibrium constant [mol$^{0.5}$]
k	Velocity constant [1/s]
l	Length [m]
$\dot{m}$	Mass flux [kg/s]
m	Mass [kg]
mf	Mass fraction [–]
n	Number [–]
Nu	Nusselt number [–]
p	Pressure [Pa]
pp	Position of the particle alongside the wall [m]
$\dot{Q}$	Heat flux [J/s]
q	Specific heat flux [J/m^{2}s]
R_s	Specific gas constant [J/kgK]
r	Radius [m]
r	radial coordinate [m]
Re	Reynolds number [–]
T	Temperature [K]
t	Time [s]
$\Delta V°$	Reaction volume [m^3/mol]
v	Velocity [m/s]
x	x-coordinate [m]

Indices

0	Ambient state
1	State 1
2	State 2
a	Available
B	Bubble
boil	Boiling
cat	Catalyst
cond	Condensation
eff	Effective
ext	External
g	Gaseous
I	Category I
i	Inner
II	Category II
III	Category III
conv	Convective
l	Liquid
m	Mixture
new	New
pore	Pore
r	Reaction partners
rkt	Reaction
T	Thiele
tot	Total
u	Used
wall	Wall

Abbreviations

CEA	Chemical equilibrium and application code

HTPB Hydroxyl-Terminated Polybutadiene
HTP High Test Peroxide

References

[1] W. Kopacz, A. Okinski, A. Kasztankiewisz, P. Nowakowski, G. Rarata, P. Makismowski, Hydrogen peroxide - a promising oxidizer for rocket propulsion and its application in solid rocket propellants, FirePhysChem 2 (2022) http://dx.doi.org/10.1016/j.fpc.2022.03.009.

[2] A. Dadieu, R. Damm, E.W. Schmidt, Raketentreibstoffe, Springer Wien, ISBN: 978-3-211-80856-6, 1969.

[3] Rocketdyne Inc., Hydrogen Peroxide Handbook, AFRPL-TR-67-144, 1967.

[4] S. May, N.M. Bierwagen, G. Poppe, C. Glaser, A. Ohndorf, Mobile hydrogen peroxide transport and storage container for worldwide rocket launches, in: Space Propulsion Conference, 2024, SP2024_230.

[5] M.C. Ventura, Long term storability of hydrogen peroxide, in: Joint Propulsion Conference & Exhibit, AIAA2005-4551, 2005.

[6] W. Reschetilowski, Handbuch Chemischer Reaktoren. Chemische Reaktionstechnik:Theoretische und praktische Grundlagen, Springer-Spektrum, ISBN: 978-3-662-56455-4, 2021.

[7] A. Pasini, L. Torre, L. Romeo, A. Cervone, L. d'Agostino, Reduced-order model for H_2O_2 catalytic reactor performace analysis, J. Propuls. Power 26 (3) (2010) http://dx.doi.org/10.2514/1.44355.

[8] S. Jung, S. Choi, S. Heo, S. Kwon, Scaling of catalyst bed for hydrogen peroxide monopropellant thrusters using catalytic decomposition modeling, Acta Astronautica 187 (2021) http://dx.doi.org/10.1016/j.actaastro.2021.06.027.

[9] D.H. Kerr, A.R. Karagozian, D. Bilyeu, D. Eckhardt, Nondeterministic analysis of monopropellant catalyst bed, J. Propuls. Power 37 (1) (2021) http://dx.doi.org/10.2514/1.B37853.

[10] S. Kang, Catalyst bed behavior of hydrogen peroxide/kerosene bipropellant thruster in monopropellant and bipropellant modes with cavitating venturi valve, Acta Astronaut. 205 (2003) http://dx.doi.org/10.1016/j.actaastro.2023.01.029.

[11] R.-J. Koopmans, J.S. Shrimpton, G.T. Roberts, A.J. Musker, A one-dimensopnal multicomponent two-fluid model of reacting packed bed including mass, momentum and energy interphase transfer, Int. J. Multiph. Flow 57 (2013) http://dx.doi.org/10.1016/j.ijmultiphaseflow.2013.06.005.

[12] R.-J. Koopmans, Modelling of Multiphase Multicomponent Chemically Reacting Flows Through Packed Beds, (Ph.D. thesis), University of Southampton, 2013.

[13] S. Reid, D. Symsons, M. Watson, Transient, multiscale, heterogenous model of hydrogen peroxide decomposition for 3D-printed catalysts, J. Propuls. Power 39 (1) (2023) http://dx.doi.org/10.2514/1.B38746.

[14] E.Q. Granado, J. Hijlkema, J.-Y. Lestrade, J. Anthoine, A new system design tool for a hybrid rocket engine, Acta Astronautica (2024) http://dx.doi.org/10.1016/j.actaastro.2024.06.031.

[15] N.M. Bierwagen, T. Eggers S. May, A. Ohndorf, Ch. Mundt, Particle-based modeling of the unsteady flow in a high-test peroxide catalytic chamber, in: Aerospace Europe Conference - EUCASS, 2023, http://dx.doi.org/10.13009/EUCASS2023-861.

[16] P.W. Atkins, Physikalische Chemie, VCH Verlagsgesellschaft mbH, ISBN: 3-527-25913-9, 1990.

[17] G.B. Wallis, One-Dimensional Two-Phase Flow, McGraw-Hill, Inc, 1969, LCCN 75–75170 67942.

[18] P. Gerlinger, Numerische Verbrennungssimulation. Effiziente Numerische Simulation Turbulenter Verbennung, Springer-Verlag, Berlin, Heidelberg, ISBN: 978-3-540-23337-4, 2005.

[19] C. Kleinstreuer, Two-Phase Flow. Theory and Applications, Taylor & Francis Books, Inc., ISBN: 1-59169-000-5, 2003.

[20] M. Ishii, T. Hibiki, Thermo-fluid Dynamics of Two-phase Flow, Springer Science+Business Media, Inc., ISBN: 0-387-28321-8, 2006.

[21] T. Moreno, J. Garcia-Serna, M.J. Cocerno, Decomposition reaction of H2o2 over Pd/C catalyst in an aqueous medium at high pressure: Detailed kinetic study and modelling, J. Supercrit. Fluids Vol. 57 (2011) http://dx.doi.org/10.1016/j.supflu.2011.04.001.

[22] D. Straub, Th. K. Wurst, Chemische Thermodynamik, in: manuscript of the lecture, Universität der Bundeswehr München, 1989.

[23] DIN Institut für Normung e. V., Determination of Specific Surface Area of Solids by Gas Adsorption -BET Method, DIN ISO 9277, 2014.

[24] M. Kieke, Implementation of Extended Chemical and Geometrical Calculation Models in The DLR-code AHRES-SHAKIRA, (student thesis), Technische Universität Braunschweig, 2017.

[25] T. Oehmichen, L. Datsevich, A. Jess, Influence of bubble evolution on the effective kinetics of heterogeneously catalyzed gas/liquid reactions, part I: Reactions with gaseous products, Chem. Eng. Technol. 33 (6) (2010).

[26] G. Schlosser, Heterogene Katalyse, Verlag Chemie GmbH, 1972.

[27] DIN Institut für Normung e. V, Bestimmung der porengrößenverteilung und der spezifischen oberflöche mesoporöser feststoffe durch stickstoffsorption, 1998, DIN 66134:1998-02.

[28] K. Hatanaka, Y. Shibauchi, Sterilization method and apparatus therefore, 1989, United states patent 4.797.255.

[29] T. Arens, F. Hettlich, C. Karpfinger, U. Kockelkorn, K. Lichtenegger, H. Stachel, Mathematik, Springer Spectrum, 2015.

[30] H. Brauer, Grundlagen der Einphasen- und Mehrphasenströmungen, Sauerländer AG, 1971.

[31] S. Ergun, Fluid flow trough packed columns, Chem. Eng. Prog. 48 (2) 1952.

[32] J.A. Tallmadge, Packed-bed pressure drop - an extension to higher Reynolds numbers, AlChE J. (1970).

[33] J. Wu, B. Yu, M. Yun, A resistance model for flow through porous media, Transp. Porous Media 71 (2008) http://dx.doi.org/10.10007/s11242-007-9129-0.

[34] VDI-Gesellschaft Verfahrenstechnik und Chemieingenieurwesen (Hrsg),, VDI-Wärmeatlas, Springer Vieweg, ISBN: 978-3-642-19981-3, 2006.

[35] N.M. Bierwagen, Regressionsratenbestimmung des brennstoffs in einem zweidimensionalen hybridraketentriebwerk mittels laufzeitmessung von ultraschallsignalen, (student thesis), Technische Universität Braunschweig, 2019.

[36] A. Dabanovic, S. May, D. Hargarten, M. Liebisch, V. Wartemann, The ALDUINA hybrid upper stage: propulsion system design and support infrastructure, in: 76th International Astronautical Congress - IAC, 2025.

[37] A. Dabanovic, J. Martin, S. May, T. Eggers, Design of a souding rocket upper stage based on the hybrid rocket engine, CEAS Space Journal (2023) http://dx.doi.org/10.1007/s12567-022-00451-2.

[38] O. Assenmacher author A. Dabanovic author G. Poppe, A. Rüttgers, Automatic outline detection for hybrid rocket static firing tests, in: 75th International Astronautical Congress - IAC, 2024.

[39] C. Cottenot, B. Boust, L. Prevost, R. Beauchet, Y. Batonneau, M. Bellenoue, Diameter of spherical alumina pt catalyst: Influence on hydrogen peroxide decomposition performance & catalytic bed ageing, Aerospace Europe Conference - EUCASS, 2023, http://dx.doi.org/10.13009/EUCASS2023-799.

[40] S. Gordon, B.J. McBride, Computer Program for Calculation of Complex Chemical Equilibrium Compositions and Applications, NASA Reference Publication 1311, 1994.

[41] TC Mess- und Regelungstechnik GmbH, Handbuch zur temperaturmessung mit thermoelementen und widerstandsthermoelementen, 2018.

[42] N.M. Riedel, J. Martin, A. Ohndorf, Ch. Mundt, Multi-phase injection through bypass: a novel catalytic chamber design, in: 75th International Astronautical Congress (IAC), 2024.

[43] B. Weigand, J. Köhler, J. Wolfersdorf, Thermodynamik Kompakt, Springer Vieweg, 2016, http://dx.doi.org/10.1007/978-3-662-49703-6.

[44] B.J. McBride, S. Gordon, Computer Program for Calulating and Fitting Thermodynamic Functions, NASA, 1992.

[45] P.J. Linstrom, W.G. Mallard (Eds.), NIST Chemistry WebBook, NIST Standard Reference Database Number, vol. 69, National Institute of Standards and Technology, 2024, http://dx.doi.org/10.18434/T4D303.

[46] A.K. Coker, Ludwig's Applied Process Design for Chemical and Petrochemical Plants, vol. 2, Elsvier Science & Technology, ISBN: 9780080942094, 2010.